Desalination and Water Treatment
www.deswater.com

doi: 10.1080/19443994.2016.1157705

57 (2016) 25301–25316
November

Taylor & Francis
Taylor & Francis Group

Modeling and optimizing of adsorption removal of Reactive Blue 19 on the magnetite/graphene oxide nanocomposite via response surface methodology

Zahra Ayazi[b,*], Zahra Monsef Khoshhesab[a], Somayeh Norouzi[a]

[a]*Department of Chemistry, Payame Noor University, Tehran 19395-4697, I.R. Iran, emails: monsefkh@yahoo.com (Z.M. Khoshhesab), s.n_1391@yahoo.com (S. Norouzi)*
[b]*Faculty of Sciences, Department of Chemistry, Azarbaijan Shahid Madani University, P.O. Box 53714-161, Tabriz, I.R. Iran, Tel./Fax: +98 41 34327500; email: ayazi@azaruniv.edu*

Received 30 August 2015; Accepted 30 January 2016

ABSTRACT

In this study, magnetite/graphene oxide (MGO) nanocomposite was prepared and applied for adsorption removal of Reactive Blue 19 (RB19). Optimization and modeling of the removal of RB19 using MGO were performed through the response surface methodology (RSM) based on central composite design (CCD). The MGO nanocomposite was synthesized by coprecipitation method. The structure and morphology of the prepared nanocomposite were characterized using X-ray diffraction, Fourier transform infrared spectroscopy, scanning electron microscopy, Brunauer–Emmett–Teller analysis and vibrating sample magnetometer (VSM). Important factors influencing the adsorption of RB19 including pH, initial concentration of RB19, adsorbent dosage, and contact time were considered as input variables for RSM. The analysis of variance showed a high correlation coefficient ($R^2 = 0.954$) between experimental and predicted responses. The removal efficiency of dye was more than 99% at the optimum condition proposed by RSM. Furthermore, the adsorption kinetic studies revealed that the adsorption process followed the pseudo-second-order model. Based on Langmuir isotherm model, the maximum adsorption capacity, q_m, was calculated to be 62.5 mg g^{-1}.

Keywords: Magnetic nanoparticles; Graphene oxide; Reactive Blue 19; Central composite design; Adsorption removal

1. Introduction

Nowadays, pollution of water resources by various pollutants is a global environmental issue. Large amount of dangerous dyes and pigments produced from dye manufacturing, textile as well as paper and pulp industries is introduced into wastewaters. It is estimated that the amount of dyes produced annually exceeds 700,000 tons, with 10–15% being discharged into wastewater [1,2]. Colors tend to persist even after the conventional removal processes which makes difficulties to treat water contamination [3,4]. The dye contaminations in water exhibit some environmental adverse effect. They tend to prevent light penetration and therefore, affect photosynthesis considerably. Additionally, the long lifetimes of dyes in water reservoirs, sometimes cause food chain contamination, resulting in adverse effects on human and animal health. Reactive Blue 19 (RB19) is an anthraquinone-based vinylsulphone

*Corresponding author.

dye, extensively used in dyeing of cellulosic fibers. It is very resistant to chemical and biological degradation due to its aromatic anthraquinone structure which is highly stabilized by resonance [5]. Regarding the chemical stability and low biodegradability of RB19, its removal from dyeing effluents and wastewaters becomes very important to decrease its impact on the environment. Diverse chemical and physical treatment procedures such as membrane separation, ozonation, photo-oxidation, electrochemical methods, and adsorption have been applied for wastewater treatment. Among these methods, adsorption-based procedure is a common applicable technique due to the unique advantages such as nontoxic, adsorbents versatility, their high adsorption capacity, cost effective, and high removal percentage in addition to regenerability of adsorbent [6].

Nowadays, nanomaterials with unique physical and chemical properties exhibit intrinsic surface activity (high surface areas) and possess various surface atoms strongly adsorb many chemical substances. Nanocomposite materials due to multifunctionality and increase in the number and type of reactive atoms are good candidates for interaction with various organic compounds that lead to outcome their efficient removal. The surface structure, size, and interparticle interaction of nanomaterials determine their unique properties and make their potential application in many areas [7,8].

Carbon-based materials are widely used for the dye removal process [9]. A recent literature review focused on the use of the graphene or graphene oxide (GO) materials as promising adsorbent materials for the removal of the dye molecules from the water [10,11]. Graphite is the basic material for preparation of individual graphene or GO nanosheets. Graphene is one-atom-thick two-dimensional (2D) layers of sp^2-bonded carbon that can be considered the "mother of all graphitic forms" of nanocarbon, including 0D buckyballs, 1D carbon nanotube, and 3D graphite [12,13]. Graphene has remarkable properties, such as huge surface area (with a calculated value of 2,630 $m^2 g^{-1}$), good chemical stability, and graphitized basal plane structure, which allow it to have strong π–π interactions with the aromatic moieties that exist in many dyes [14,15]. This suggests that graphene would be a good adsorbent for removing dye pollutants. However, graphene sheets usually suffer from serious agglomeration and restacking during utilization, due to the π–π interactions between neighboring sheets, leading to a great loss of effective surface area and consequently a lower adsorption capacity than expected [16]. In this regard, application of GO instead of graphene can lead to the superior results. Exfoliation of graphite oxide by ultrasonication results in single-layered GO nanosheets. GO due to the large surface area, surface functionalities containing oxygen such as carboxylic, hydroxyl, carbonyl, and epoxide groups, and high water solubility is a material of great interest in adsorption-based technologies as well as in other fields [17,18]. The electrostatic interaction of the GO with the ionic adsorbates makes it a material of choice for adsorption of charged species [11,19]. However, the major difficulty of its application is its small particle size and the high dispersibility in aqueous solutions, which leads to its difficult separation from solution after adsorption process via filtration and/or centrifugation. The development of magnetic adsorbents could be a solution to this problem which leads to the convenient magnetic separation after adsorption. Magnetic adsorbents have advantages such as their easy phase separation in aqueous solutions and the capability of treating large amount of wastewater in short period of time. Magnetic separation based on the superparamagnetic Fe_3O_4 is much more efficient, convenient, and economic which have found many interesting applications nowadays [20,21]. Compared with traditional methods, such as filtration, centrifugation, or gravitational separation, magnetic separation requires less energy and can achieve better separation especially for adsorbents with small particle size. Therefore, fabrication of magnetite/graphene oxide (MGO) nanocomposites by combining GO with magnetite nanoparticles should offer an effective approach to overcome the separation problems associated with GO. At the same time, loading of the magnetite nanoparticles can avoid or decrease the possibility of serious agglomeration and restacking of the graphene sheets, and consequently provide a higher available surface area and enhancement of adsorption capacity, owing to the spacing effect of the magnetite nanoparticles between the neighboring graphene nanosheets.

In this work, Fe_3O_4/GO nanocomposite was synthesized due to the coprecipitation of $FeCl_2$ and $FeCl_3$ in the presence of GO. As mentioned, the hybrid of GO and magnetic nanoparticle can create promising advantages especially magnetically separation of sorbent. The capability of the magnetite graphene oxide nanocomposite for the adsorption of RB19 was investigated. This prepared sorbent has been not applied for RB19 up to now. Therefore, the investigation of RB19 adsorption onto MGO can be notified as interesting aspect of this research. The behavior of adsorption was modeled and optimized on effects of pH, the initial RB19 concentration, contact time, and adsorbent dose using response surface methodology (RSM) based on central composite design (CCD). Finally, isothermal behavior and kinetic studies on the adsorption of RB19 were investigated.

2. Experimental procedures

2.1. Materials

Graphite fine powder was purchased from Loba Chemie (Mumbai, India). Chemicals including ferric chloride hexahydrate ($FeCl_3{\cdot}6H_2O$), ferrous chloride tetrahydrate ($FeCl_2{\cdot}4H_2O$) sulfuric acid, NH_4OH, hydrochloric acid, and sodium hydroxide were all obtained from Merck (Germany). Sodium nitrate and H_2O_2 (30% v/v) were supplied from Loba Chemie. Distilled water was used throughout the experiments. An anionic dye Reactive Blue 19 (RB19) also known as Remazol Brilliant Blue R ($C_{22}H_{16}O_{11}N_2S_3Na_2$, M.W: 626.5 g mol^{-1}) was selected as model compound (the structure of RB19 is presented in Fig. 1). This anionic dye was provided by Dyestar Co. (Germany).

2.2. Instruments

A Shimadzo UV–vis spectrophotometer (Tokyo, Japan) was used to measure the concentration of RB19 at λ_{max} = 595 nm. A Metrohm 827 pH/Ion meter (Switzerland) with a combined glass–calomel electrode was used for adjustment of test solution pH. Sample agitation was performed on a shaker (Sahand.T.a., Iran). The graphite oxide was suspended in water through ultrasonication (model: MM3010, OSCAR Ultrasonic, India) to obtain GO nanosheets.

A permanent magnet of Nd–Fe–B (8.0 cm × 6.0 cm × 1.6 cm) was applied for magnetic separation. The morphology of the samples was studied using scanning electron microscope (SEM) (KYKY-EM3200, China). Fourier transform infrared (FTIR) spectroscopic experiment was carried out on a JASCO 4200 (Japan) apparatus. X-ray diffraction (XRD) evaluations were performed using a Philips, PW1800 (Netherland) instrument. The sorbents were analyzed for their Brunauer–Emmett–Teller (BET)-specific surface area (calculated using the BET standard method) and pore size distribution (calculated using the Barrett–Johner–Halenda (BJH) method) using a Belsorb mini (II) analyzer. Magnetic characterization of the prepared nanocomposite was performed using vibrating sample magnetometer (VSM) MDKFD instrument (Iran).

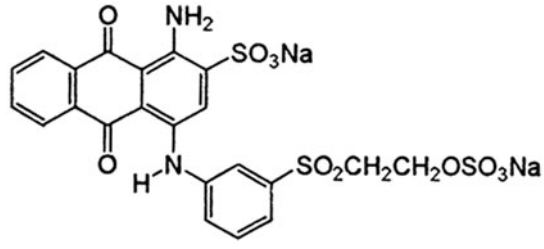

Fig. 1. Chemical structure of RB19.

2.3. Preparation of GO

GO was prepared using graphite powder according to the Hummers and Offeman method [22]. Briefly, 1 g of graphite powder and 0.5 g sodium nitrate were added to 23 mL of concentrated H_2SO_4 in a 500-mL flask. The prepared mixture was stirred at 1,200 rpm in an ice bath for 1 h. $KMnO_4$ (3 g) was then added slowly with stirring. Then, the flask was removed from ice bath to keep the temperature of the reaction mixture in room temperature. After 2 h, 46 mL of deionized water was added slowly to this mixture and temperature was kept at 98˚C using an oil bath. After 15 min, 100 mL of deionized water and 100 mL of 30% H_2O_2 solution were added. For purification, the mixture was washed by rinsing and centrifugation with HCl (5% v/v) followed by deionized water for several times. The residue thus obtained was dried in an air oven at 50˚C for 72 h.

2.4. Synthesis of MGO nanocomposite

Fe_3O_4/GO was synthesized by chemical coprecipitation method. In a typical synthesis, GO (1 g) was dispersed in 50 mL of water by sonication for 10 min in order to exfoliate GO nanosheet. Then, 3.5 g $FeCl_3{\cdot}6H_2O$ and 1.25 g of $FeCl_2{\cdot}4H_2O$ were dissolved in 50 mL of water and the solution was sonicated for 5 min. 150 mL water was added into the 500 mL fask and was put into an oil bath at 70˚C. Then, the two prepared solutions were added into flask under a nitrogen flow. After that, ammonia solution (28%) was added dropwise until the pH of solution reached 10 for synthesis of magnetite nanoparticles. After 45 min, the black precipitate was separated by applying an external magnetic field and washed with water several times, and finally was dried in an oven at 50˚C for 24 h.

2.5. Batch adsorption experiments

In order to estimate the adsorption characteristics of RB19 onto magnetic graphene oxide nanocomposite, batch adsorption studies were carried out in 25 mL of dye solution containing different amount of adsorbent. The initial pH of the solution was adjusted with 1 M HCl or 1 M NaOH solution using a pH meter and the solutions were agitated using a shaker. At the end of desired exposure time, an external magnet

(8.0 cm × 6.0 cm × 1.6 cm) was easily and quickly applied to the bottom of the beaker and the Fe_3O_4/GO nanocomposite was aggregated from the solution and the concentration of remaining RB19 in the supernatant was determined by spectrophotometric method at λ_{max} value of 595 nm.

2.6. Experimental design

CCD which is used widely in RSM experimental design was employed to evaluate the individual and interactive effects of controllable variables on the output response. Four parameters affecting the removal condition ($k = 4$) have been introduced as RSM input variables, including initial concentration of RB19, pH, adsorbent amount, and contact time, which their experimental ranges in coded and actual values are presented in Table 1. The removal percentage (R %) was calculated as response of model. CCD for studying the removal process, with four input variables consists of 31 experiments with 16 (2^k) orthogonal two-level full-factorial design points (coded as ±1), 8 ($2k$) axial points (or star point coded as $\pm\alpha = 2.0$) and 7 replications of the central points to provide an estimation of the experimental error variance. The design of experiments and experimental data analysis were performed using Minintab 16 software. The adequacy and significance of the model were determined by analysis of variance (ANOVA). The quality of the polynomial model equation was judged statistically by the correlation coefficient, R^2 and its statistical significance was evaluated by F-test. p-values less than 0.05 were considered to be statistically significant.

2.7. Measurements of dye uptake

The dye concentration was determined using photometry method at maximum wavelength over working concentration. The efficiency of dye removal was determined at different experimental condition according to CCD method. The dye removal percentages (R %) were calculated using the following equation (Eq. (1)):

$$R\,\% = \frac{C_0 - C_t}{C_0} \times 100 \tag{1}$$

where C_0 (mg L^{-1}) and C_t (mg L^{-1}) is the concentration of dye at initial and after time t, respectively. In order to investigate adsorption isotherms and also adsorption kinetic, the equilibrium adsorption capacity (q_e) (mg g^{-1}) and adsorption capacity at certain time (q_t) (mg g^{-1}) were calculated according to following equations (Eqs. (2) and (3)):

$$q_e = \frac{(C_0 - C_e)V}{W} \tag{2}$$

$$q_t = \frac{(C_0 - C_t)V}{W} \tag{3}$$

where V (L) is the volume of solution and W (g) is the weight of adsorbent.

3. Results and discussion

3.1. Characterization of Fe_3O_4/GO nanocomposite

To obtain the structural information about MGO, XRD characterization was conducted for MGO, GO, and Fe_3O_4 nanoparticles (Fig. 2). Six diffraction lines were observed in the representative XRD pattern of Fe_3O_4 at $2\theta = 30.2^\circ$, 35.6°, 43.3°, 53.7°, 57.3°, and 62.8°. These diffraction lines can be assigned to the pure cubic spinel crystal structure of Fe_3O_4 with cell constant $a = 8.39$ Å (JCPDS card No. 19-0629) [23,24]. As presented in the XRD pattern of the GO, two well-defined peak at $2\theta = 10.9^\circ$ and 26.1° are related to the GO and graphite, respectively. Interestingly, in the XRD pattern of MGO nanocomposite, the characteristic peak of GO located at 10.4° disappeared, which suggests that the GO sheets are disordered and there were spaces between them [24]. In addition, the diffraction peak related to the parent graphite was observed, which attributed to the presence of graphite in the final product. The remaining diffraction peaks are related to the Fe_3O_4 nanoparticle.

Table 1
Actual and coded values of independent variables applied for response surface method

Effect	Symbol	$-\alpha$	−1	0	+1	$+\alpha$
Contact time (min)	x_1	10	40	70	100	130
pH	x_2	3	4.5	6	7.5	9
Sorbent amount (mg)	x_3	50	100	150	200	250
Dye concentration (mg L^{-1})	x_4	50	150	250	350	450

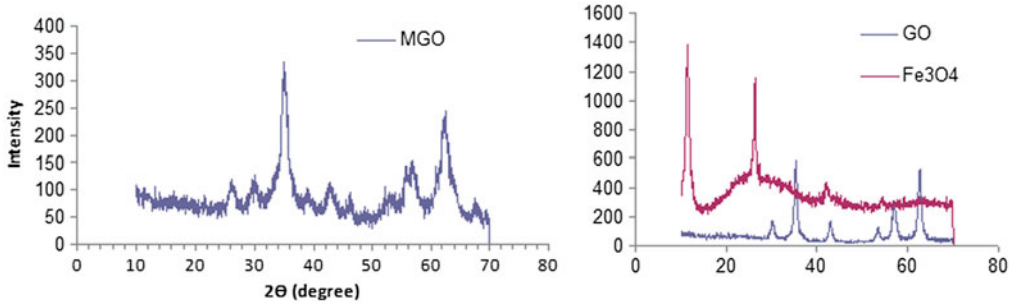

Fig. 2. XRD patterns of GO, Fe_3O_4 nanoparticles, and the synthesized MGO.

FTIR of the parent graphite oxide as well as of the prepared nanocomposite are presented in Fig. 3. GO and Fe_3O_4/GO nanocomposite both showed the O–H stretching vibration adsorption peak at 3,401 cm^{-1}. As to GO (curve a), the peaks at 1,721 cm^{-1} was the C=O stretching vibration peak of carboxyl and carbonyl; the peak at 1,616 cm^{-1} was attributed to the stretching vibration of aromatic C=C; the peaks at 1,225 and 1,046 cm^{-1} were ascribed to the C–O stretching vibration of epoxy group and alkoxy [25]. These peaks demonstrated the existence of carboxyl, epoxy group, and alkoxy in GO. The Fe–O characteristic stretching vibration peak at 578 cm^{-1} was observed in curve b, which proved that Fe_3O_4 NPs was successfully anchored onto GO nanosheet [26].

A SEM image of the GO and MGO nanocomposite is presented in Fig.4. Fig. 4(a) presents the nanosheets of GO which are in different size and shape but their thickness are same. According to Fig. 4(b) related to the MGO nanocomposite, the magnetic nanoparticles are observable that are attached to the surface of the GO nanosheets. The nanosize of prepared magnetic nanaoparticles is evident. Furthermore, it is clear that Fe_3O_4 nanoparticles are well distributed throughout the prepared magnetic nanocomposite.

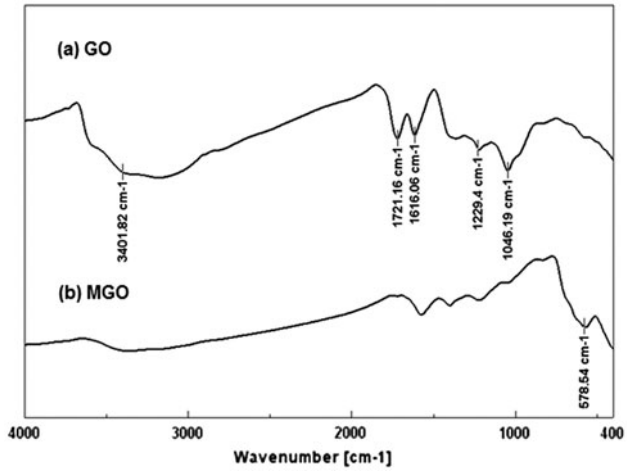

Fig. 3. FTIR spectra of (a) GO and (b) MGO.

The sorbents were analyzed for their BET-specific surface area and pore size distribution. Nitrogen sorption isotherm is an efficient way for providing information about the pore system of materials. Concept of the BET theory is an extension of the Langmuir theory, which is a theory for monolayer molecular adsorption, to multilayer adsorption. The N_2 adsorption/desorption isotherms of magnetic GO sample at −196°C (77 K) is shown in Fig. 5. According to the IUPAC classification, the isotherm is of type II, indicating unrestricted monolayer–multilayer adsorption. This suggests that adsorption of N_2 for the sorbent materials is moderate or, on the other hand, the main adsorption process may be ascribed to a van der Waals force. The filling of the micropores with nitrogen molecules occurs in the initial part of the type II isotherm, whereas a complete adsorption of N_2 as a monolayer onto the surface of sorbent material is shown by the plateau of the adsorption isotherm. After this point, a large uptake of N_2 is observed close to the saturation pressure and it is assumed that multilayer adsorption takes place on mesopores, macropores, and the external surface [27]. The changes in the isotherm slope at point $P/P_0 > 0.1$ indicate that the monolayer coverage stage is completed and that multilayer adsorption is about to begin [28]. The BET surface area, pore volumes, and pore size of the MGO sample are summarized in Table 2.

The BJH procedure, which permits a better characterization of mesoporosity, was applied to obtain the pore size distribution from nitrogen desorption data. The pore size distribution is represented by the derivative $d(V_p)/d(d_p)$ as a function of pore diameter, where V_p is the pore volume and d_p is the pore diameter. For fresh sorbent, mesopores with an average pore size of 16 nm appeared to be the major

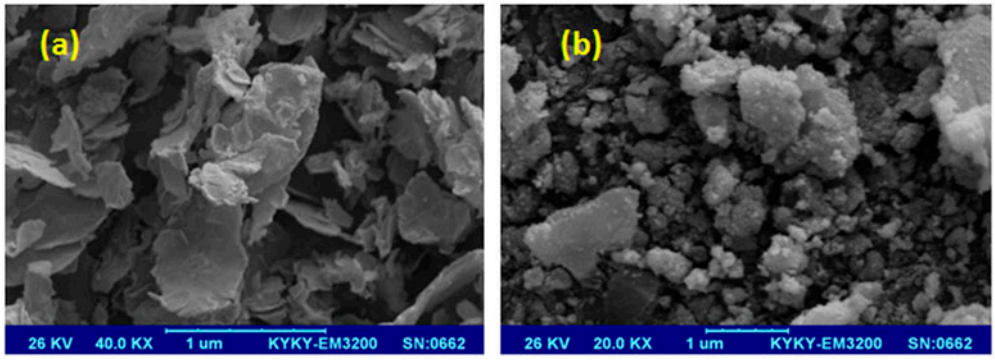

Fig. 4. SEM images of (a) graphene oxide and (b) Fe_3O_4/GO nanocomposite.

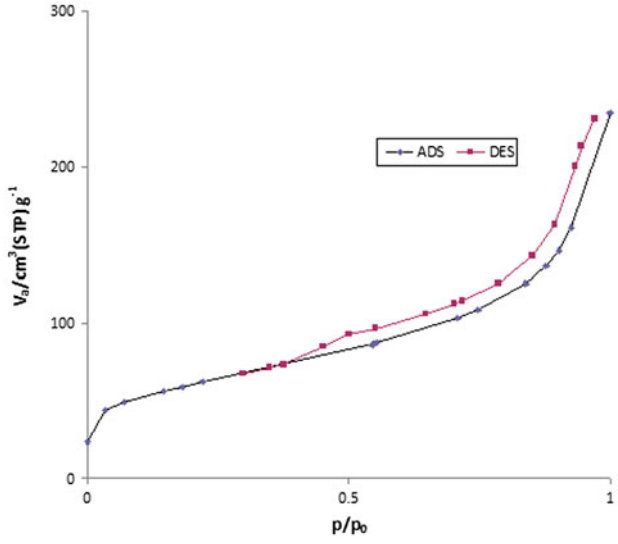

Fig. 5. BET adsorption and desorption isotherms for MGO.

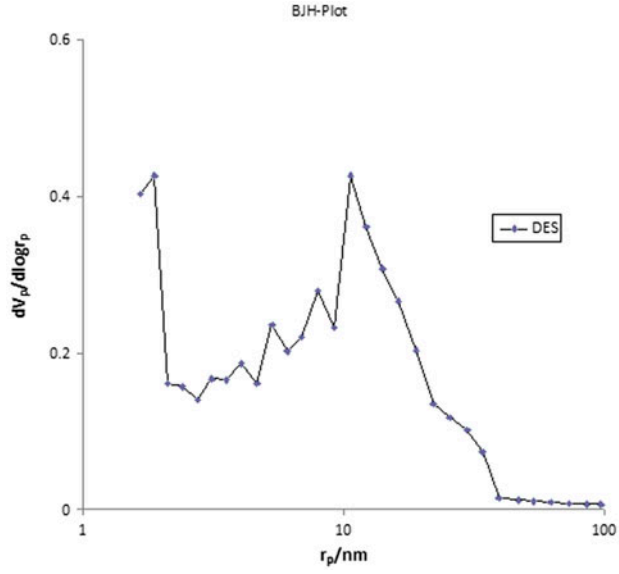

Fig. 6. Pore size distributions of prepared magnetic graphene oxide.

Table 2
Textural properties of magnetic graphene oxide

V_m (cm^3(STP) g^{-1})	49.518
$a_{s,BET}$ (m^2 g^{-1})	215.53
Total pore volume (P/P_0 = 0.990) (cm^3 g^{-1})	0.3483
Mean pore diameter (nm)	6.465

contributor to the total pore volume. The pore-size distribution of MGO sorbent is shown in Fig. 6.

Magnetic characterization of the prepared nanocomposite was done using VSM at room temperature, with a magnetic field in the range of −8,000 to 8,000 Oe, where parameters as saturation magnetization (M_s), and coercive field (H_c) were evaluated. Coercive force or coercivity is the force required to remove the residual magnetism from the material. Fig. 7 shows VSM plot of MGO at 300 K. The hysteresis loop does not display magnetic remanence, and thus the nanoparticles are considered to be superparamagnetic (H_c = 0 Oe). The magnetization saturation (M_s) of the MNPs was 5.76 emu g^{-1}. Accordingly, it can be concluded that the prepared magnetic graphene oxide is superparamagnetic without coercivety and also has magnetic characteristic for separation of nanocomposite from aquatic media.

3.2. RSM model development

Generally, RSM is defined as a statistical method that uses quantitative data from appropriate experiments to solve multivariate equation. Main aim of RSM is to obtain an optimal response. A second-order (quadratic) polynomial response surface model (Eq. (4)) can be used to fit the experimental results obtained by CCD. This model, also known as regression equation,

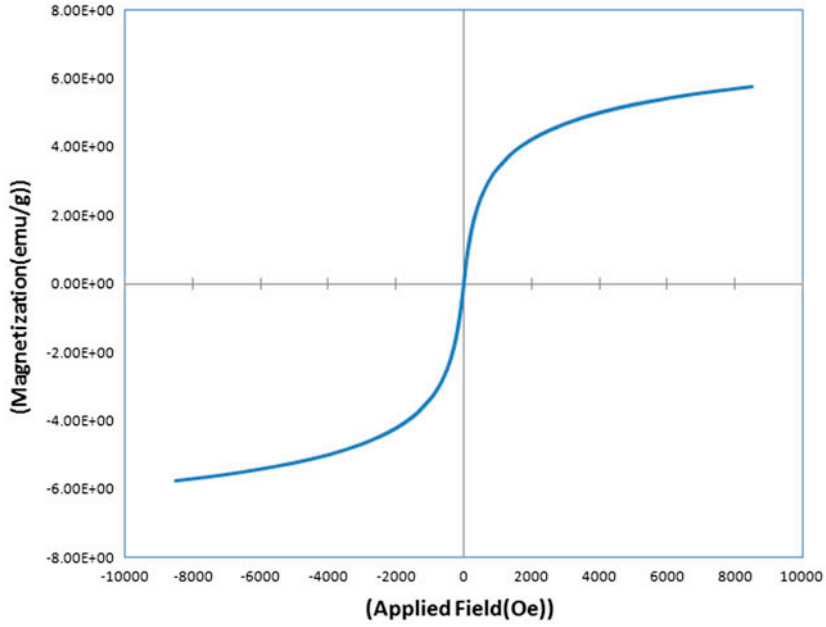

Fig. 7. Magnetization vs. applied magnetic field for magnetic graphene oxide.

describes a polynomial approximation of experimental results with following relationship:

$$Y = b_0 + \sum_{i=1}^{n} b_i x_i + \sum_{i=1}^{n} b_{ii} x_{ii}^2 + \sum_{i=1}^{n} \sum_{j=i+1}^{n} b_{ij} x_i x_j \quad (4)$$

where Y is the predicted response, x_i denotes the coded levels of the factors, b_0 is a constant and b_i, b_{ii}, and b_{ij} are the regression coefficients for the linear, quadratic, and interaction effects, respectively. These coefficients were calculated by means of ordinary least square.

The regression equation with coded variables for describing the removal percentage of Reactive Blue 19 from aquatic solution using MGO sorbent can be presented as follow (Eq. (5)):

$$\begin{aligned} Y = {} & 84.7771 + 3.2125x_1 - 0.4092\,x_2 + 15.1758\,x_3 \\ & - 13.6600\,x_4 - 1.2903\,x_1^2 + 1.2797\,x_2^2 - 5.0953\,x_3^2 \\ & - 1.5791\,x_4^2 + 0.6950\,x_1\,x_2 + 0.8550\,x_1\,x_3 \\ & + 1.3925\,x_1\,x_4 + 0.3750\,x_2\,x_3 + 0.0525\,x_2\,x_4 \\ & - 8.1025\,x_3\,x_4 \end{aligned} \quad (5)$$

where x_1, x_2, x_3, and x_4 are contact time, pH, sorbent amount, and dye concentration respectively. ANOVA was performed to evaluate the significance and adequacy of the model and the obtained results are presented in Table 3. The significance of the second-order regression models were determined by the Fisher's variance ratio test (F-test), lack of fit (LOF) test, and coefficients of determination between the experimental and predicted values (R^2 and Adjusted R^2). Fisher F-values of regressions is defined as the ratio of regression mean square due to the residual error. According to the results tabulated in Table 3, F-value is 49.54 which is much higher than the tabulated F-value (2.352 at 95% significance). If the regression model predicts the experimental results suitably, F-value should be higher than the tabulated value. Additionally, p-values lower than 0.05 (at the significance level of 95%) confirm that the regression of model is statistically significant. In developed model for removal of RB19, the p-value was 0.000, showing the significance of regression. Furthermore, the LOF test is other criterion for evaluating the model which is performed by comparing the residual with pure error achieved from replication of

Table 3
ANOVA for the developed model

Source	DF[a]	Seq SS[b]	Adj MS[c]	F-value	p-value
Regression	14	122,614	87,582	49.54	0.000
Residual error	16	2,829	1,768	–	–
Lack-of-fit	10	244.2	24.42	3.79	0.058
Pure error	6	38.7	6.45	–	–
Total	30	12,544.3	–	–	–

[a]Degree of freedom.
[b]Sum of squares.
[c]Adjusted mean square.

experiment at the central level of factors [29]. In this case, despite regression of model, if the *F*-value of LOF is lower than tabulated value or the related *p*-value is greater than 0.05 (at the significance level of 95%), the regression will be adequately significant. According to the results tabulated in Table 3, the *p*-values of LOF test were 0.058 which confirm the insignificant LOF and adequacy of the model. Moreover, the comparison of experimental and predicted removal efficiencies showed that the correlation coefficients, R^2 and Adjusted R^2 values were 97.74 and 95.77% for developed model. The values of R^2 are desirable, because it has been suggested that for a good fit of a model, R^2 should be at least 80% [30].

Additionally, for evaluating the adequacy of the developed model, the difference between predicted and experimental responses (residuals) can be applied for investigating the significance of the model graphically. Residuals are considered as unexplained variations by model and they will occur based on a normal distribution, if the model is a good predictor [31]. Fig. 8(a) depicts the normal probability vs. internally studentized residuals. As shown in Fig. 8(a), there is no obvious dispersal for the obtained data points, which is favorable. The normal probability plot should follow a relatively straight line. Additionally, random dispersal of the residuals can be seen in the plots of residuals vs. predicted dye removal (%) or fitted values in Fig. 8(b) and run number in Fig. 8(d), demonstrating a good fitness between predicted and experimental dye removal. Moreover, the histogram of residuals was depicted in Fig. 8(c) indicated rather normal distribution of residuals.

3.3. Effect of variables on removal efficiency

In order to determine the importance and effectiveness of each term in the developed model, corresponding values of Student's *t* distribution and related *p*-values (Table 4) are considered. The greater *t*-value and/or the smaller *p*-value (less than 0.05 at 95% significance) for a coefficient show the more significant influence of the coefficient [32,33]. According to the Table 4, the insignificant coefficient in Eq. (5) (the coefficient with *p*-value greater than 0.05) was eliminated and the mentioned equation was rewritten as Eq. (6):

$$Y = 84.7771 + 3.2125\,x_1 + 15.1758\,x_3 - 13.6600\,x_4 - 5.0953\,x_3^2 - 8.1025\,x_3\,x_4 \quad (6)$$

As shown in Eq. (6), the model for removal of RB19 consisted of three main effects, one curvature effect, and one interaction effect. In order to determine the significance of each factor, the percentage effect of each term on the response (known as Pareto analysis) can be calculated using the following equation (Eq. (7)) [34]:

$$P_i = \frac{b_i^2}{\sum_{i=1}^{n} b_i^2} \times 100 \quad (7)$$

where P_i is the percentage effect of each factor and b_i is the corresponding coefficient. According to the results, shown in the Fig. 9, the most effective term is the main effect of sorbent amount (b_3, 43.64%). After the sorbent amount, the dye concentration was more significant than other factors in removal efficiency (b_4, 35.33%). The main effect of exposure time (b_1, 1.95%), interaction of sorbent amount and dye concentration (b_{34}, 12.42%), and curvature effect of sorbent amount (b_{33}, 4.9%) are also important. Sorbent amount is shown as effective factor with positive sign which indicates the increase in removal efficiency with increase in sorbent dosage (Figs. 10(b), 11(a) and (c)). Note that the greater adsorbent dosage lead to the availability of the more surface area and adsorption sites, and therefore the more adsorption can be obtained. Figs. 10(a) and 11(a) indicated that at any exposure time from 10 to 130 min and at any solution pH from 3 to 9, the removal was increased by increase in adsorbent amount and there is no interaction of sorbent amount with contact time and pH. But the interaction of dye concentration and sorbent amount is dominant. When the dye concentration is in level of 50 mg mL^{-1}, low level of sorbent amount has led to favorable removal; however, when the dye concentration is increased, low level of sorbent amount has led to the insufficient dye removal and it is not enough to remove all dye molecules.

Dye initial concentration is one of the important parameters influencing removal efficiency with negative sign; the effect of this factor can be indicated using the Pareto analysis and also response surface plot (Figs. 9, 10(c), 11(a) and (c)). According to these figures, dye concentration has a negative effect on removal efficiency and increasing the dye concentration causes decrease in removal efficiency. At higher initial dye concentrations, lower dye removal is probably attributed to the saturation of adsorptive sites on the surface of MGO nanocomposite.

3.4. Numerical optimization

In order to carry out numerical optimization, the values of independent parameters were set to the studied range, while the dependent parameter (dye

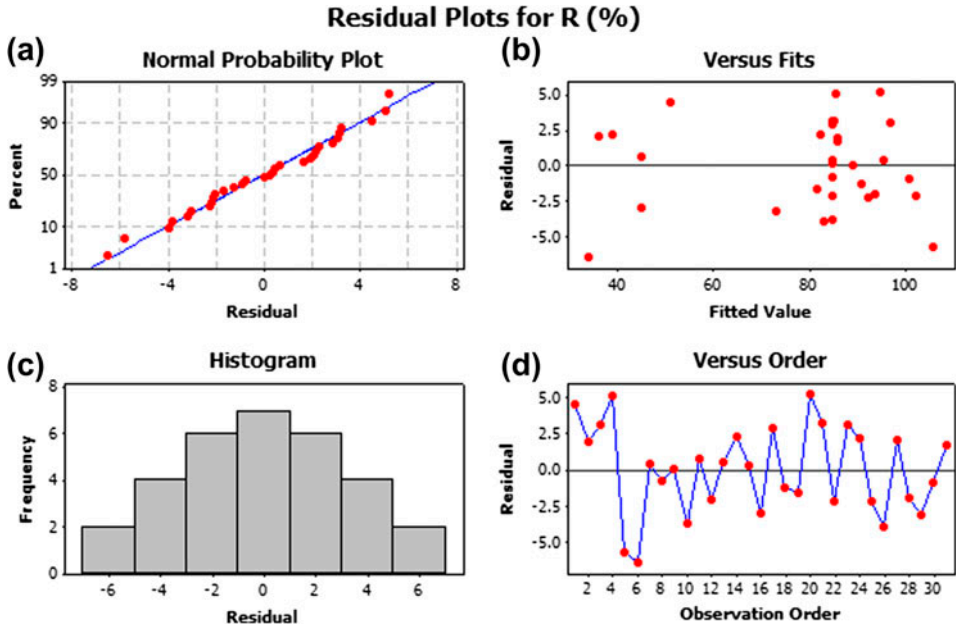

Fig. 8. Residual plots for removal efficiency of RB19: (a) normal probability plots of residuals, (b) residuals vs. fits plots, (c) histogram of residuals, and (d) residuals vs. observation order.

Table 4
Estimated model coefficients for extraction and desorption process and corresponding *t* and *p*-values

Coefficient	Coefficient estimate	*t*-value	*p*-value	Remark
b_0	84.7771	53,344	0.000	–
b_1	3.2125	3.743	0.002	S[a]
b_2	−0.4092	−0.477	0.640	
b_3	15.1758	17.681	0.000	HS[b]
b_4	−13.6600	−15.915	0.000	HS
b_{11}	−1.2903	−1.641	0.120	
b_{22}	1.2797	1.627	0.123	
b_{33}	−5.0953	−6.480	0.000	HS
b_{44}	−1.5791	−2.008	0.062	
b_{12}	0.6950	0.661	0.518	
b_{13}	0.8550	0.813	0.428	
b_{14}	1.3925	1.325	0.204	
b_{23}	0.3750	0.357	0.726	
b_{24}	0.0525	0.050	0.961	
b_{34}	8.1025	7.807	0.000	HS

[a]Significant.
[b]Highly significant.

removal) was set to achieve maximum dye removal. As a result, the maximum dye removal of 99% was obtained at an initial dye concentration of 420 mg L^{-1}, adsorbent dosage of 250 mg, contact time of 66.72 min, and pH 3. Besides, confirmatory experiments were carried out according to the optimum operational parameters to validate the obtained results. The results of experiments revealed a dye removal of 99% under optimum operational parameters, demonstrating the accuracy of the model for predicting dye removal.

3.5. Adsorption isotherm

Adsorption isotherms are important for the description of how adsorbate interacts with adsorbent surface. Adsorption equilibrium isotherm is designed

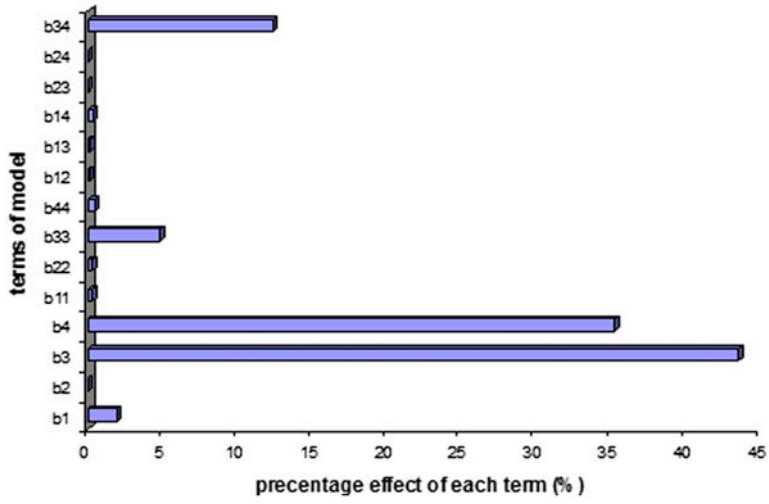

Fig. 9. Percentage effect of each model term obtained using Pareto analysis.

based on mathematical relation of the amount of adsorbed target per gram of adsorbent (q_e (mg g^{-1})) to the equilibrium non-adsorbed amount of dye in solution (C_e (mg L^{-1})) at fixed temperature. Isotherm studies are divided to well-known models such as Langmuir [35], Freundlich [36], and Temkin [37] based on well-known conditions. In the present study, these isotherms have been applied for explanation of the adsorption data. The Langmuir isotherm describes monolayer sorption due to a surface of a finite number of identical sites. This isotherm assumes that uptake of molecules occurs on a homogenous surface without any interaction between adsorbate molecules and is expressed in the linear form as Eq. (8):

$$\frac{C_e}{q_e} = \frac{1}{b\,q_m} + \frac{C_e}{q_m} \tag{8}$$

where C_e is the equilibrium non-adsorbed amount of dye in solution (mg L^{-1}) and q_e the amount adsorbed at equilibrium (mg g^{-1}). The Langmuir constants q_m (mg g^{-1}) represent the monolayer adsorption capacity and b (L mg^{-1}) relates the heat of adsorption.

The Freundlich isotherm is valid for the heterogeneous surface energies by multilayer adsorption and is expressed in linear form as Eq. (9):

$$\ln q_e = \ln K_f + \frac{1}{n} \ln C_e \tag{9}$$

where K_f (mg g^{-1}) is approximately an indicator of the adsorption capacity, and $1/n$ is the adsorption intensity and an indicator for the favorability of adsorption. As the value of $n > 1$ represents favorable adsorption condition [38].

The Temkin isotherm equation assumes that the heat of adsorption of all the molecules in layer decreases linearly with coverage due to adsorbentadsorbate interactions, and that the adsorption is characterized by a uniform distribution of the bonding energies, up to some maximum binding energy. The linear form of Temkin isotherm is written as Eq. (10):

$$q_e = B_1 \ln K_T + B_1 \ln C_e \tag{10}$$

where $B_1 = RT/b$ is related to the heat of adsorption, T is the absolute temperature in Kelvin, and R (8.314 J mol^{-1} K^{-1}) is the universal gas constant [39]. K_T is the equilibrium binding constant (L mol^{-1}) corresponding to the maximum binding energy. A plot of q_e vs. ln C_e enables the determination of the isotherm constants B_1 and K_T from the slope and the intercept, respectively.

In this study, the Langmuir, Freundlich, and Temkin isotherms for the adsorption of RB19 onto MGO nanocomposite were studied by exposing 250 mg of nanocomposite to the 25 ml of RB19 solutions with various initial concentrations of 400–750 mg L^{-1} at pH 3. After 66.72 min, the concentration of RB19 in the solution was measured and the isotherm parameters were calculated using Eqs. (8)–(10), and the detailed parameters of adsorption isotherms are listed in Table 5. The results showed that Langmuir isotherm fits almost well with the experimental values. This means that the adsorption of RB19 takes place at specific homogeneous sites and a one-layer adsorption onto MGO surface. Also, there are no interactions

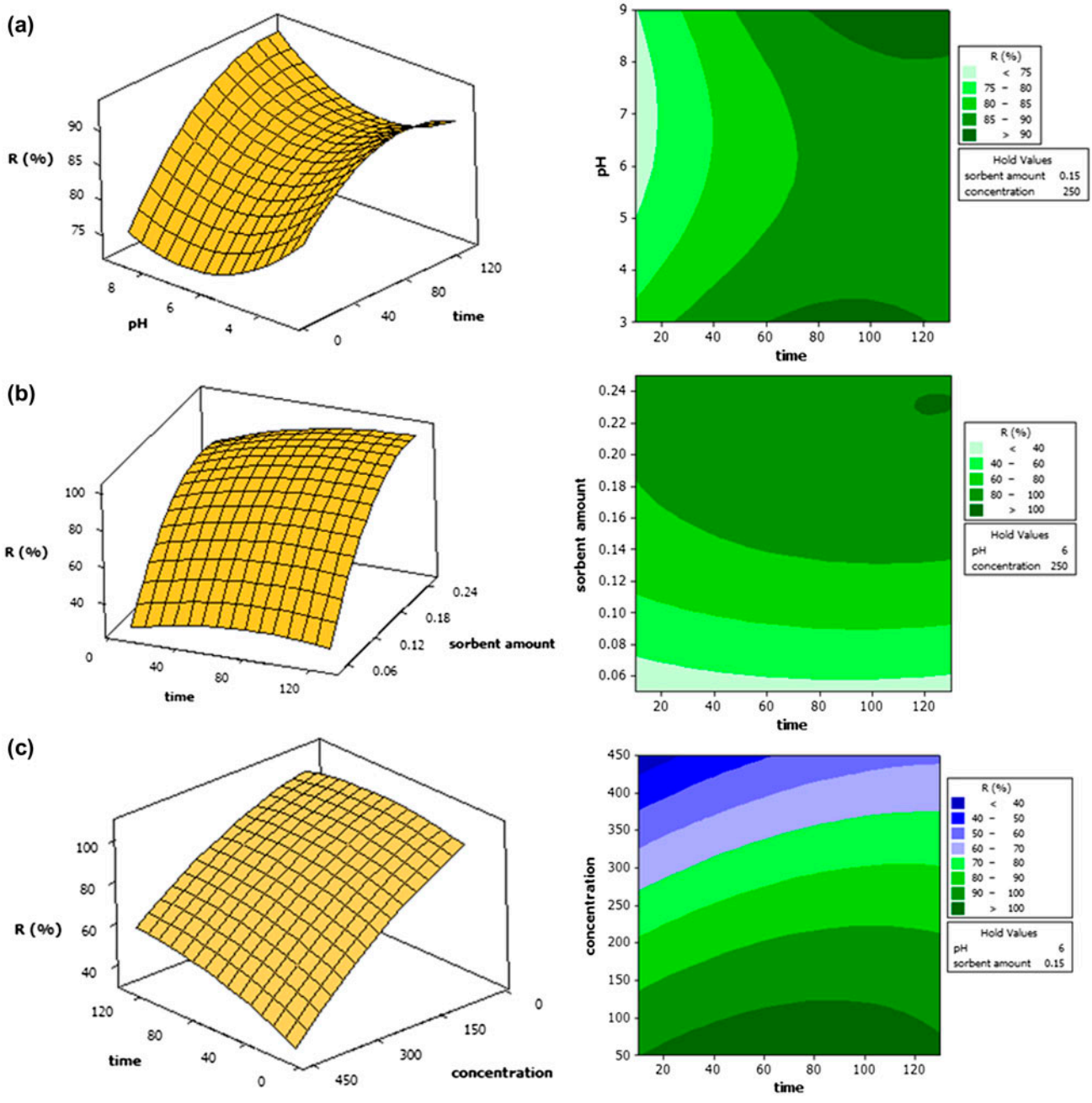

Fig. 10. Response surface and counter plots of predicted RB19 removal percentage as a function of (a) contact time and pH, (b) contact time and sorbent amount, and (c) contact time and dye concentration, keeping other variables at central point levels.

between adsorbate molecules on adjacent sites. Based on Langmuir model, Langmuir constant q_m was calculated to be 62.5 mg g^{-1}.

3.6. Adsorption kinetics

The kinetic parameters are helpful for the prediction of adsorption rate, which gives important information for the efficiency of adsorption. Hence, pseudo-first-order [40], second-order [41], pseudo-second-order [42], Elovich [43,44], and intraparticle diffusion [42,45] kinetic models were studied for adsorption of RB19 onto Fe_3O_4/GO nanocomposite. The correlation coefficients, R^2, show the level of consistency between the experimental and calculated

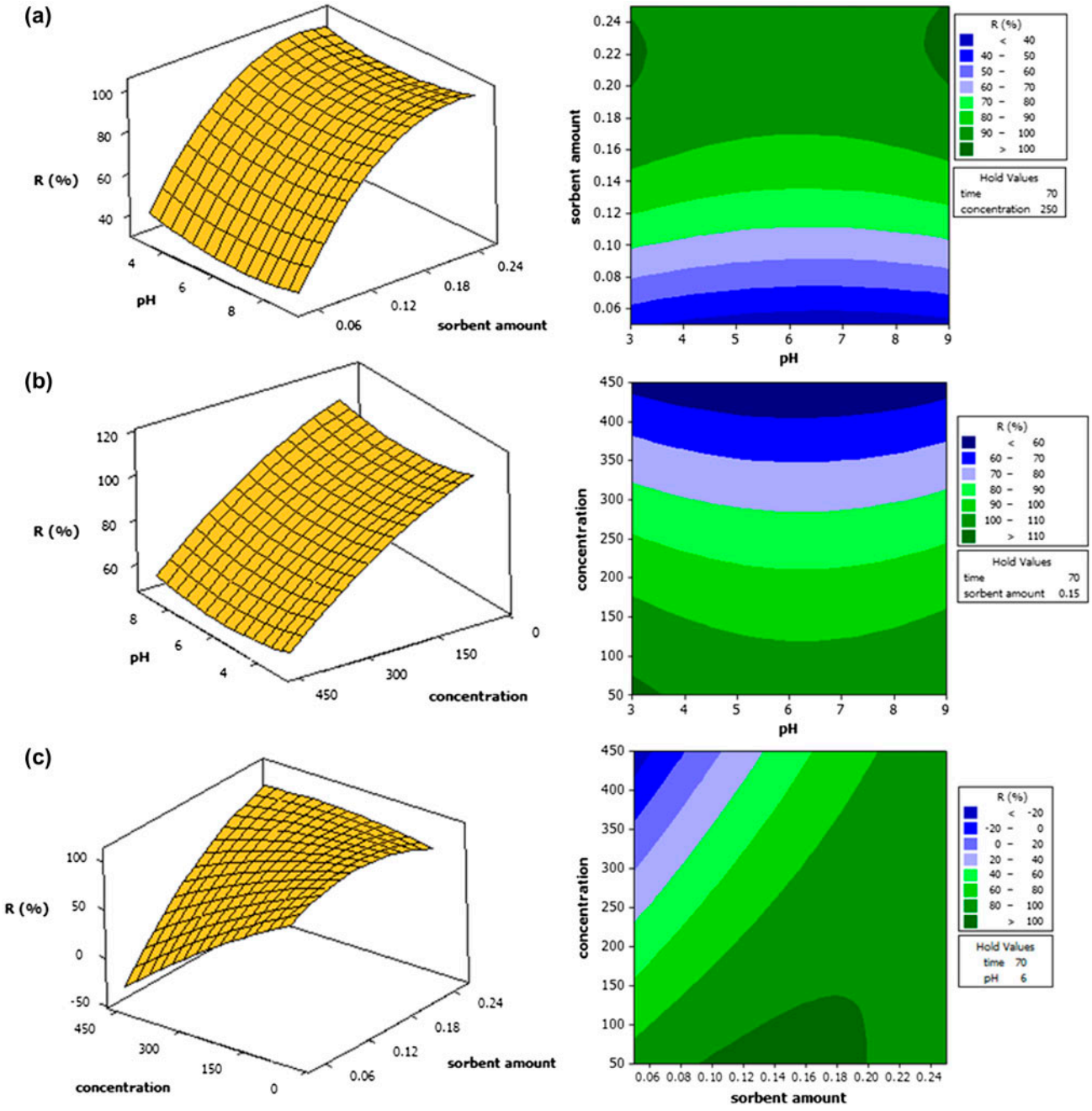

Fig. 11. Response surface and counter plots of predicted RB19 removal percentage as a function of (a) pH and sorbent amount, (b) pH and dye concentration, and (c) sorbent amount and dye concentration, keeping other variables at central point levels.

values. The higher R^2 value which is closer to one shows the better applicability of the model.

For kinetic evaluation of RB19 adsorption, 250 mg of the MGO nanocomposite was added to the 25 mL of RB19 solution with initial concentration of 420 mg L^{-1} at pH 3 and room temperature. According to the Fig. 12, adsorption of RB19 was rapidly increased up to 15 min and thereafter was increased gradually up to the studied time of 80 min. Therefore, it can be concluded that the rate of RB19 adsorption onto the MGO nanocomposite was greater in the initial time, then gradually decreased and remained almost constant. The first rapid increase in binding capacity is due to the presence of vacant site available

Table 5
Isotherm parameters and correlation coefficients calculated by various adsorption models onto 250 mg of Fe_3O_4/GO in 25 mL, pH 3, and room temperature

Langmuir	q_m	Maximum adsorption capacity reflected a complete monolayer (mg g^{-1})	62.5 (±0.6)
	b	Langmuir constant or adsorption equilibrium constant (L mg^{-1})	0.115 (±0.004)
	R^2	Correlation coefficient	0.9885
Freundlich	n	Isotherm constant indicate the empirical parameter (g L^{-1})	13.88 (±0.02)
	K_F	Isotherm constant indicate the capacity parameter (mg g^{-1})	37.7 (±0.5)
	R^2	Correlation coefficient	0.7064
Temkin	B_1	Related to the heat of adsorption	8.96 (±0.0.8)
	K_T	Equilibrium binding constant (L mg^{-1})	4.84 (±0.03)
	R^2	Correlation coefficient	0.8961

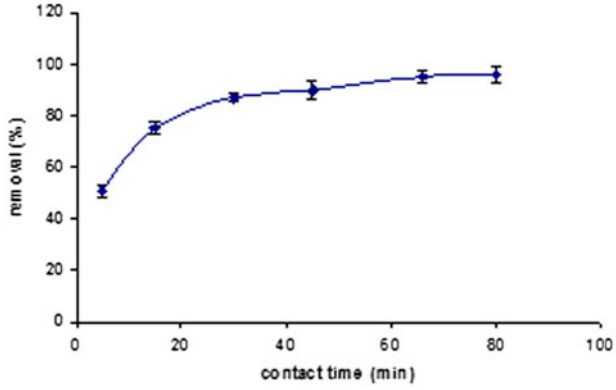

Fig. 12. Effect of contact time on the removal percentage of RB19 by Fe_3O_4/GO nanocomposite at concentration of RB19) (420 mg L^{-1}), pH 3, adsorbent dose (250 mg), batch volume (25 ml), room temperature.

at the initial stage. Generally, when adsorption involves a surface interaction process, the initial adsorption is fast. Then, with decrease in available adsorption sites adsorption would be slower. In this study, in order to determine the best kinetic model which fits the adsorption experimental data, the Lagergren pseudo-first-order, the pseudo-second-order, and the second-order models according to Eqs. (11)–(13), were examined.

$$\log \frac{q_e - q_t}{q_e} = \log q_e - \frac{K_L}{2.303} t \tag{11}$$

$$\frac{t}{q_t} = \frac{1}{K' q_e^2} + \frac{t}{q_e} \tag{12}$$

$$\frac{1}{q_e - q_t} = \frac{1}{q_e} + K_2 t \tag{13}$$

where K_L is the Lagergren pseudo-first-order rate constant (min^{-1}); K' is the pseudo-second-order rate constant (g mg^{-1} min^{-1}) and K_2 is the second-order rate constant (g mg^{-1} min^{-1}); q_e and q_t are the amounts of solute adsorbed (mg g^{-1}) at equilibrium and at time t, respectively.

The Elovich equation is another rate equation which is based on the adsorption capacity is given as follows (Eq. (14)) [44]:

$$q_t = \frac{1}{\beta} \ln(\alpha\beta) + \frac{1}{\beta} \ln(t) \tag{14}$$

Plot of q_t vs. $\ln(t)$ should yield a linear relationship with a slope of $(1/\beta)$ and an intercept of $(1/\beta)$ $\ln(\alpha\beta)$ if the Elovich model is the best kinetic model. The Elovich constants obtained from the slope and the intercept of the straight line are reported in Table 6.

Another alternative method for kinetic study of an adsorption process is intraparticle diffusion [45]. This model is based on transport of target species from aqueous solution to the adsorbents by intraparticle diffusion according to the well-known equation (Eq. (15)):

$$q_t = K_{dif} t^{1/2} + C \tag{15}$$

The values of K_{dif} and C were calculated from the slopes of q_t vs. $t^{1/2}$ and their values are reported in Table 5. The values of q_t were found to give two lines part with values of $t^{1/2}$ and the rate constant K_{dif} directly evaluated from the slope of the second regression line. When the value of C was equal to zero which in this case, the plot of q_t vs. $t^{1/2}$ passes through the origin, intraparticle diffusion is the sole

Table 6
Adsorption kinetic parameters at different initial RB19 onto 250 mg of MGO in 25 mL at pH 3, room temperature and RB19 concentration of 420 mg L^{-1}

Pseudo-first-order kinetic	K_1	Rate constant of pseudo-first-order adsorption (L min^{-1})	0.039 (±0.001)
	$q_{e(calc)}$	Equilibrium capacity (mg g^{-1})	11.5 (±0.2)
	R^2	Correlation coefficient	0.8878
Second-order kinetic	k_2	Second-order rate constant of adsorption (g (mg $min)^{-1}$)	90.5 (±0.4)
	$q_{e(calc)}$	Equilibrium capacity (mg g^{-1})	−0.375 (±0.007)
	R^2	Correlation coefficient	0.9747
Pseudo-second-order kinetic	K'	Pseudo-second-order rate constant (g mg^{-1} min^{-1})	0.0072 (±0.0002)
	q_e	Equilibrium capacity (mg g^{-1})	43.48 (±0.03)
	R^2	Correlation coefficient	0.9992
Intraparticle diffusion	K_{dif}	Rate constant of intraparticle diffusion (mg g^{-1} $min^{-0.5}$)	2.28 (±0.04)
	C	Intercept of intraparticle diffusion	23.9 (±0.5)
	R^2	Correlation coefficient	0.7795
Elovich	β	Desorption constant (g mg^{-1})	0.179 (±0.003)
	α	Initial adsorption rate (mg (g $min)^{-1}$)	153 (±3)
	R^2	Correlation coefficient	0.8980
$q_{e(exp)}$		Experimental data of the equilibrium capacity (mg g^{-1})	40.8 (±0.8)

rate-limiting step [46]. This phenomenon shows that the intraparticle diffusion model may be the controlling factor in determining the kinetic of the process [47]. The distance of R^2 values (Table 5) from unity indicates the non applicability of this model that rejects the rate-limiting step is the intraparticle diffusion process.

The values of several kinetic parameters and correlation coefficients (R^2) obtained from applied different kinetic models for adsorption of RB19 onto MGO nanocomposite are tabulated in Table 6. The highest correlation coefficient (R^2) is related to the pseudo-second-order adsorption model. In addition, the calculated values of $q_{e(cal)}$ obtained from pseudo-second-order kinetics model are very closer to the experimental values of $q_{e(exp)}$ (Table 6) obtained from experimental data. According to these results the pseudo-second-order adsorption mechanism is predominant.

3.7. Reusability study

In order to investigate the reusability of the adsorbent, different desorbing solvents including methanol, ethanol, ethyl acetate, acetonitrile, and their binary mixture with water were applied for the desorption of adsorbed RB19. The desorption process was performed by adding 10 mL of the each solvent to the dye-loaded adsorbent and shaking the mixture for 15 min. After desorption, the dye concentration in the desorbed solution was measured and the percentage of dye desorbed from the adsorbent was determined. Except ethanol/water mixed solvent, the desorption efficiency using the remaining solvents was lower than 20%. Therefore, different ratios of ethanol/water mixtures (1:3, 1:2, and 1:4, v/v) were further evaluated. Concerning to the results, the desorption efficiency was more than 90% when ethanol/water (2:3 v/v) was used as desorbing solvent. Therefore, an ethanol/water (2:3 v/v) binary mixed solvent was used as proper eluent for the desorption process and investigation of the reusability of the adsorbent. The results showed that the removal efficiency was nearly constant during the five cycles of adsorption/desorption experiments, indicating the presented MGO nanocomposite could be reusable adsorbent.

4. Conclusions

The synthesis of Fe_3O_4/GO nanocomposite was performed by chemical coprecipitation of ferrous chloride and ferric chloride in the presence of GO nanocomposite dispersion at alkaline media. The application of prepared nanocomposite was investigated as an adsorbent for the removal of RB19 from aqueous solutions. The effects of pH, adsorbents dosage, initial dye concentration, and contact time on the removal of RB19 were investigated through batch experiments using CCD. Langmuir, Freundlich, and Temkin models were applied for the experimental equilibrium data and results showed that better fit was obtained with Langmuir model. The adsorption capacity, q_m, from this model was found to be 62.5 mg g^{-1}. The batch adsorption kinetic was studied and the pseudo-second-order kinetic model was able to best describe the adsorption kinetic of the RB19 onto Fe_3O_4/GO nanocomposite. The reusability studies revealed that the MGO nanocomposite can be

applied for five cycles of adsorption/desorption experiments without decrease in removal efficiency. Finally, the novel nanocomposite designed in this study is distinguished by significantly higher stability, adsorption capability, reusability, and versatile applicability making it an industrially viable, economical, and successful product to removal of RB19 from solutions.

Acknowledgments

The authors would like to thank the Azarbaijan Shahid Madani University (Tabriz, Iran) and Payame Noor University (Qazvin, Iran) for their instrumental and financial supports.

References

[1] K. Hunger, Industrial Dyes: Chemistry, Properties, Applications, Wiley-VCH, Weinheim, Germany, 2003.
[2] R.M. Christie, Environmental Aspects of Textile Dyeing, Woodhead Publishing, Great Abington, Cambridge, 2007.
[3] M. Ghaedi, S. Hajati, F. Karimi, B. Barazesh, G. Ghezelbash, Equilibrium, kinetic and isotherm of some metal ion biosorption, J. Ind. Eng. Chem. 19 (2013) 987–992.
[4] M. Visa, C. Bogatu, A. Duta, Simultaneous adsorption of dyes and heavy metals from multicomponent solutions using fly ash, Appl. Surf. Sci. 256 (2010) 5486–5491.
[5] M. Siddique, R. Farooq, A. Shaheen, Removal of reactive blue 19 from wastewaters by physicochemical and biological processes—A review, J. Chem. Soc. Pak. 33 (2011) 284–293.
[6] M. Tuzen, K.O. Saygi, C. Usta, M. Soylak, *Pseudomonas aeruginosa* immobilized multiwalled carbon nanotubes as biosorbent for heavy metal ions, Bioresour. Technol. 99 (2008) 1563–1570.
[7] W.T. Tsai, Y.M. Chang, C.W. Lai, C.C. Lo, Adsorption of basic dyes in aqueous solution by clay adsorbent from regenerated bleaching earth, Appl. Clay Sci. 29 (2005) 149–154.
[8] E. Eren, B. Afsin, Investigation of a basic dye adsorption from aqueous solution onto raw and pre-treated bentonite surfaces, Dyes Pigm. 76 (2008) 220–225.
[9] P. Sivakumar, P.N. Palanisamy, Adsorption studies of basic red 29 by a non-conventional activated carbon prepared from *Euphorbia antiquorum* L, Int. J. Chem. Technol. Res. 1 (2009) 502–510.
[10] X.Y. Pang, F. Gong, Study on the adsorption kinetics of acid red 3B on expanded graphite, E-J. Chem. 5 (2008) 802–809.
[11] P. Bradder, S.K. Ling, S. Wang, S. Liu, Dye adsorption on layered graphite oxide, J. Chem. Eng. Data 56 (2011) 138–141.
[12] K.S. Novoselov, A.K. Geim, S.V. Morozov, D. Jiang, Y. Zhang, S.V. Dubonos, I.V. Grigorieva, A.A. Firsov, Electric field effect in atomically thin carbon films, Science 306 (2004) 666–669.
[13] A.K. Geim, K.S. Novoselov, The rise of graphene, Nat. Mater. 6 (2007) 183–191.
[14] Q. Su, S. Pang, V. Alijani, C. Li, X. Feng, K. Müllen, Composites of graphene with large aromatic molecules, Adv. Mater. 21 (2009) 3191–3195.
[15] K. Loh, Q. Bao, P.K. Ang, J. Yang, The chemistry of graphene, J. Mater. Chem. 20 (2010) 2277–2289.
[16] R. Zacharia, H. Ulbricht, T. Hertel, Interlayer cohesive energy of graphite from thermal desorption of polyaromatic hydrocarbons, Phys. Rev. B 69 (2004) 155406.
[17] D. Li, M.B. Müller, S. Gilje, R.B. Kaner, G.G. Wallace, Processable aqueous dispersions of graphene nanosheets, Nat. Nanotechnol. 3 (2008) 101–105.
[18] S. Park, R.S. Ruoff, Chemical methods for the production of graphenes, Nat. Nanotechnol. 4 (2009) 217–224.
[19] G.K. Ramesha, A. Vijaya Kumara, H.B. Muralidhara, S. Sampath, Graphene and graphene oxide as effective adsorbents toward anionic and cationic dyes, J. Colloid Interface Sci. 361 (2011) 270–277.
[20] J. Sun, Q. Liang, Q. Han, X. Zhang, M. Ding, One-step synthesis of magnetic graphene oxide nanocomposite and its application in magnetic solid phase extraction of heavy metal ions from biological samples, Talanta 132 (2015) 557–563.
[21] Y.P. Chang, C.L. Ren, J.C. Qu, X.G. Chen, Preparation and characterization of Fe_3O_4/graphene nanocomposite and investigation of its adsorption performance for aniline and p-chloroaniline, Appl. Surf. Sci. 261 (2012) 504–509.
[22] W.S. Hummers, R.E. Offeman, Preparation of graphitic oxide, J. Am. Chem. Soc. 80 (1958) 1339–1339.
[23] H.P. Cong, J.J. He, Y. Lu, S.H. Yu, Water-soluble magnetic-functionalized reduced graphene oxide sheets: In situ synthesis and magnetic resonance imaging applications, Small 6 (2009) 169–173.
[24] M. Zhang, D. Lei, X. Yin, L. Chen, Q. Li, Y. Wang, T. Wang, Magnetite/graphene composites: Microwave irradiation synthesis and enhanced cycling and rate performances for lithium ion batteries, J. Mater. Chem. 20 (2010) 5538–5543.
[25] V. Chandra, J. Park, Y. Chun, J.W. Lee, I.C. Hwang, K.S. Kim, Water-dispersible magnetite-reduced graphene oxide composites for arsenic removal, ACS Nano 4 (2010) 3979–3986.
[26] C.C. Huang, H.S. Li, C.H. Chen, Effect of surface acidic oxides of activated carbon on adsorption of ammonia, J. Hazard. Mater. 159 (2008) 523–527.
[27] F. Rouquerol, J. Rouquerol, K. Sing, Assessment of Surface A, Adsorption by Powders and Porous Solids, Academic Press, London, 6 (1999) 165–189.
[28] Z. Zhang, W. Qu, J. Peng, L. Zhang, X. Ma, Z. Zhang, W. Li, Comparison between microwave and conventional thermal reactivations of spent activated carbon generated from vinyl acetate synthesis, Desalination 249 (2009) 247–252.
[29] M.S. Bhatti, A.S. Reddy, A.K. Thukral, Electrocoagulation removal of Cr(VI) from simulated wastewater using response surface methodology, J. Hazard. Mater. 172 (2009) 839–846.
[30] A.R. Amani-Ghadim, S. Aber, A. Olad, H. Ashassi-Sorkhabi, Optimization of electrocoagulation process for removal of an azo dye using response surface methodology and investigation on the occurrence

of destructive side reactions, Chem. Eng. Process. Process Intensif. 64 (2013) 68–78.
[31] L.A. Sarabia, M.C. Ortiz, Response surface methodology, in: S.D. Brown, R. Tauler, B. Walczak (Eds.), Comprehensive Chemometrics, Elsevier, Oxford, 2009, p. 345.
[32] Z. Ayazi, P. Rafighi, Preparation and application of a carbon nanotube reinforced polyamide-based stir bar for sorptive extraction of naproxen from biological samples prior to its spectrofluorometric determination, Anal. Methods 7 (2015) 3200–3210.
[33] A.I. Khuri, J.A. Cornell, Response Surface: Design and Analysis, Dekker, New York, NY, 1987.
[34] P.D. Haaland, Experimental Design in Biotechnology, Marcel Dekker, New York, NY, 1989.
[35] I. Langmuir, The adsorption of gases on plane surfaces of glass, mica and platinum, J. Am. Chem. Soc. 40 (1918) 1361–1403.
[36] H.M.F. Freundlich, Uber die adsorption in losungen, Z. Phys. Chem. 57 (1906) 385–470.
[37] M.J. Temkin, V. Pyzhev, Kinetics of ammonia synthesis on promoted iron catalysts, Acta Physiochim. URSS 12 (1940) 217–222.
[38] H.Y. Zhu, Y.Q. Fu, R. Jiang, J. Yao, L. Xiao, G.M. Zeng, Novel magnetic chitosan/poly(vinyl alcohol) hydrogel beads: Preparation, characterization and application for adsorption of dye from aqueous solution, Bioresour. Technol. 105 (2012) 24–30.
[39] G. Akkaya, A. Özer, Biosorption of Acid Red 274 (AR 274) on *Dicranella varia*: Determination of equilibrium and kinetic model parameters, Process Biochem. 40 (2005) 3559–3568.
[40] S. Lagergren, Zur theorie der sogenannten adsorption gelöster stoffe (About the theory of so-called adsorption of soluble substances), Kungliga Svenska Vetenskapsakademiens. Handlingar 24 (1898) 1–39.
[41] A. Olad, F. Farshi Azhar, A study on the adsorption of chromium (VI) from aqueous solutions on the alginate-montmorillonite/polyaniline nanocomposite, Desalin. Water Treat. 52 (2014) 2548–2559.
[42] S. Rengaraj, Y. Kim, C.K. Joo, J. Yi, Removal of copper from aqueous solution by aminated and protonated mesoporous aluminas: Kinetics and equilibrium, J. Colloid Interface Sci. 273 (2004) 14–21.
[43] S.H. Chien, W.R. Clayton, Application of Elovich equation to the kinetics of phosphate release and sorption in soils, Soil Sci. Soc. Am. J. 44 (1980) 265–268.
[44] J. Zeldowitsch, Uber den mechanismus der katalytischen oxidation von CO an MnO_2, Acta Physiochim. URSS 1 (1934) 364–449.
[45] P. Chingombe, B. Saha, R.J. Wakeman, Sorption of atrazine on conventional and surface modified activated carbons, J. Colloid Interface Sci. 302 (2006) 408–416.
[46] K. Srinivasan, N. Balasubramanian, T.V. Ramakrishan, Studies on chromium removal by rice husk, Ind. J. Environ. Health 30 (1988) 376–387.
[47] Y.S. Ho, G. McKay, D.A.J. Wase, C.F. Forster, Study of the sorption of divalent metal ions on to peat, Adsorpt. Sci. Technol. 18 (2000) 639–650.